The Flexible Microwave Payload-2: A SDR-Based GNSS-Reflectometer and *L*-Band Radiometer for CubeSats

Joan Francesc Munoz-Martin ⓘ, *Student Member, IEEE*, Lara Fernandez Capon, *Student Member, IEEE*, Joan Adria Ruiz-de-Azua ⓘ, *Student Member, IEEE*, and Adriano Camps ⓘ, *Fellow, IEEE*

Abstract—This article presents the FMPL-2 on board the FSS-Cat mission, the 2017 ESA Small Sentinel Satellite Challenge and overall Copernicus Masters Competition winner. FMPL-2 is a passive microwave instrument based on a software-defined radio that implements a conventional global navigation satellite system—Reflectometer and an *L*-band radiometer, occupying 1 U of a 6 U CubeSat. The article describes the FSSC at mission context, the payload design and implementation phases, the tests results in a controlled environment, and finally the calibration algorithms applied to the downloaded data in order to extract the appropriate geophysical parameters: sea-ice coverage, sea-ice thickness (SIT), and low-resolution soil moisture. This article covers the overall payload design, from a high-level block diagram down to single-component specifications from both hardware and software points of view. The main block of the instrument is based on the combination of an FPGA, which virtualizes a dual-core ARM processor, where most of the calculus are performed, and a software-defined radio module, in charge of I/Q data demodulation. The article also explains the design and implementation of a signal conditioning board required for the correct operation and calibration of both instruments.

Index Terms—Cubesats, GNSS-R, *L*-band, radiometry, RFI, sea ice, soil moisture (SM).

I. INTRODUCTION

NANOSATELLITES technology is growing, thanks notably to the advances in the miniaturization of the electronics and the telecommunications industry. These advances have translated into significantly smaller and lighter satellites, with much lower power consumption and reduced cost as compared to traditional ones. The number of satellites launched is increasing steadily since 2010 [1], notably due to CubeSat launches.

A one unit (1 U) CubeSat [2] is a 10-cm-sized cube, weighting up to 1.33 kg, which includes all the subsystems as in any other satellite. A CubeSat is specified by its "units," i.e., 1 U, 2 U, 3 U, and 6 U. Nowadays, despite there are larger CubeSats, the largest standardized CubeSat is the 6 U, about $30 \times 20 \times 10$ cm^3, and weighing ∼8 kg [2]. The original CubeSat "standard" was conceived to develop a quick and cost-effective solution to reduce the development time, to make space accessible to universities and research institutes. Nowadays governments and space agencies start looking at CubeSats standards, as a cheap way to test new technologies and as a proof-of-concept of new techniques [3], [4].

New companies and university startups start using CubeSats for communications and Earth Observation [1]: Planet Labs, a US company with more than 350 3 U CubeSats carrying optical imagers, or Spire Global with more than 100 3 U CubeSats carrying a GNSS radio occultation payload.

FMPL-2 has been designed, implemented, and tested in the UPC Nano-Satellite and Small Payloads Laboratory (UPC NanoSat-Lab [5]), and it can be considered an evolution of the PYCARO payload on board ^{3}Cat-2 [6], and the FMPL-1 on board 3Cat-4 [7].

A. FSSCat Mission Overview

FSSCat is an Earth Observation and technology demonstration mission proposed by UPC. It was the 2017 ESA Small Sentinel Satellite Challenge, and overall 2017 Copernicus Masters Competition winner. FSSCat is composed by two six-unit CubeSats: ^{3}Cat-5/A and ^{3}Cat-5/B. The "A" spacecraft is composed by the FMPL-2, a dual passive microwave remote sensing payload (GNSS-R and *L*-band microwave radiometer), and an RF/optical intersatellite link payload. ^{3}Cat-5/B is composed by the same RF/optical intersatellite link payload, while the remote sensing payload is Cosine's Hyperscout-2 [8] hyperspectral and thermal infrared imager.

The goal of FSSCat mission is to provide almost full coverage (there is a $\approx 4°$ latitude gap near the geographic poles due to the orbit inclination) of both the north and south poles providing sea-ice concentration (SIC) and SIT products from the data acquired from FMPL-2. SIC is derived from the shape of the
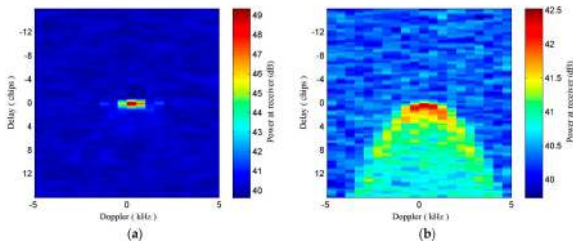
Fig. 1. Example of two DDMs from UK TDS-1 satellite over (a) sea ice and (b) ocean [22].

delay-Doppler maps (DDM) (e.g., see [9, Fig. 1]) retrieved by the GNSS-R processor of the instrument. SIT is derived from the *L*-band radiometry data [10], combined with SIC or sea-ice extent from other sensors (i.e., SAR, cGNSS-R, or Ku/Ka microwave radiometry).

The SIC product from GNSS-R has an improved spatial resolution over ice, as the reflection comes from the first Fresnel zone (i.e., 300 m from spaceborne instrument [11]), and not from the glistening zone. This improved resolution allows a precise edge detection between ice and ocean at poles. Furthermore, the combination of SIC and SIT products from GNSS-R and *L*-band radiometry sensors in a CubeSat constellation will help to enhance the amount of data collected and reduce the revisit time, which is needed to monitor and understand the evolution of sea ice [12]. Moreover, it is expected that FMPL-2 will provide also the capability to detect water ponds over sea ice, due to the expected sharp increase of the reflected power.

Finally, FSSCat will also provide low-resolution soil moisture (SM) maps over selected targets (i.e., nonpolar areas), which will be down-scaled using the hyperspectral data from Hyperscout. The pixel downscaling technique has been successfully applied to SMOS and SMAP data [13], [14]. Starting from a native resolution of SMOS data at ~ 50 km, it has been successfully downscaled overland to 1 km using optical VNIR imagery. The approach in FSSCat is the same, trying to achieve the same downscaling factor of $\sim \times 50$, which means from antenna footprint of $\sim 580 \times 385$ km (depending on final orbit) down to $\sim 12 \times 8$ km, which is comparable with most polar products from the high-frequency channels of microwave radiometers.

In the following sections, the GNSS-R and microwave radiometry techniques used are described.

B. cGNSS-R

The GNSS-R part of FMPL-2 is based on the conventional GNSS-R (cGNSS-R) technique, which is the most extended technique, used in ground-based [15], airborne [16], and spaceborne [17] instruments since the 2000 s. cGNSS-R is based on the acquisition of the GNSS-reflected signals over the earth's surface, which produce signal wavefronts depending on the reflected surface. Each signal wavefront has a different delay (τ) and Doppler (ν) that depends on the geometry [18]. The point that has the minimum path between the satellite, the surface, and the antenna is called the specular reflection point. When the surface is flat, most of the reflected power is coming from

a region around this point (first Fresnel zone). As the surface becomes rougher, more signal wavefronts scattered around the specular point are received by the antenna. The area from where these reflected signal wavefronts are received is the so-called glistening zone, and it depends not only on the roughness, but also on the height, and the elevation angle [19].

The distribution of the received signals in the delay and Doppler domains can be studied using the DDM [18] as

$$\left\langle |Y_{xy}(\tau,\nu)|^2 \right\rangle = \left\langle \left| \frac{1}{T_c} \int_0^{T_c} x(t)y^*(t-\tau)e^{-j2\pi\nu t}dt \right|^2 \right\rangle \tag{1}$$

where x and y are the complex signals to be cross correlated, T_c is the coherent integration time. In conventional GNSS-R, $x(t)$ is the received scattered signal, and $y(t)$ is the locally generated replica of the code transmitted by the navigation satellite. Fig. 1 shows two examples of DDM from a spaceborne instrument and over different scattering surfaces. Over ice, the coherent components dominate and the observation has a better spatial resolution [20]. Over the rough ocean surface, the scattering is mostly incoherent [21].

After the success of the UK-DMC GNSS-R experiments, the UK TechDemoSat-1 (TDS-1) included the first mission carrying a GNSS-R payload: the Space GNSS Receiver—Remote Sensing Instrument (SGR-ReSi) [17], [23]. The mission successfully provided measurements over ocean, land, and ice to demonstrate the capabilities of cGNSS-R for several applications, such as sea-ice detection [9], [24] or SM [25]. The second mission devoted to GNSS-R is the NASA Cyclone Global Navigation Satellite System mission, which uses similar receivers to those in TDS-1 to process the DDMs [26], and retrieves wind speed over the oceans, to monitor the hurricane evolution over the sea surface.

C. *L-Band Radiometry*

All materials at a physical temperature different from 0 K emit thermal radiation in a specific wavelength. The measure of its intensity is known as brightness temperature (T_B).[1] At *L*-band and near nadir, water brightness temperature depends on the concentration of water (i.e., SM) or the water state (i.e., liquid or ice).

The sea-ice FMPL-2 measurements are based on the retrieve of T_B over polar areas, and then apply the method described in [27] and [10]. The physical principle based on the fact that a sea-ice layer over the ocean surface affects the overall brightness temperature. While the ocean brightness temperature is about 100 K, the sea-ice layer increases the overall brightness temperature as a function of its thickness, as detailed in Fig. 2.

Other factors influencing the ice brightness temperature are its salinity, roughness, temperature profile... ESA's SMOS mission provided the data that demonstrated the capability to infer sea-ice thickness (see [28]), in addition to the mission primary goals: SM and ocean salinity.

---

[1]The noise power collected by an antenna is $N_A = k_B \cdot T_A \cdot B$, where k_B is the Boltzmann's constant, and T_A is the antenna temperature ($T_A \approx T_B$ for a narrow pencil beam antenna), and B is the noise bandwidth.
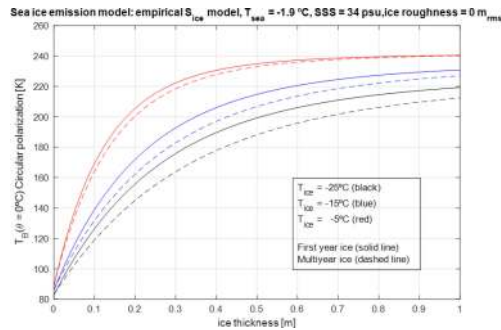
Fig. 2.   Sea-ice thickness as a function of the measured brightness temperature by a circular polarized antenna at L-band according to the model used in [10].

Fig. 3.   Flexible microwave payload 2 block diagram.

D. Soil Moisture

Besides the sea-ice-related products, FSSCat also aims at providing SM products over certain land target areas. SM data will be retrieved by the combination of the microwave radiometry data at L-band (FSSCat/A data) and multispectral imagery (e.g., MODIS or FSSCat/B Hyperscout data) by means of pixel downscaling [14]. Combining the land surface temperature, the normalized difference vegetation index, and the antenna brightness temperatures of SMOS over certain angular ranges, the SM resolution can be improved down to 1 km, from the initial 40 km of the L-band radiometer.

II. FMPL-2 HARDWARE AND SOFTWARE DESIGN

The FMPL-2 performs cGNSS-R [11] by means of the direct correlation of the GNSS signals collected by the nadir-looking antenna, with all the available codes transmitted by the satellites in view and for a reduced set of Doppler bins, for both GPS $L1$ C/A and Galileo E1 signals. The cGNSS-R processor is highly configurable in terms of incoherent integration, Doppler cuts, and maximum satellites to be observed. However, changing those parameters out of the default ones impacts on the amount of DDM per second that this processor generates.

For the radiometric measurements, the payload follows a total power radiometer (TPR) architecture with frequent internal calibrations using: an active cold load (ACL) and a matched load at known physical temperatures. Moreover, the signal collected by the antenna is evaluated using a normality test to check the presence of interference [29].

As detailed in Fig. 3, the FMPL-2 is composed by the following four modules.

1) The payload antennas (#1 in Fig. 3) are composed by two antennas: A zenith-looking $L1$-band right-hand circular polarization patch antenna for the direct GNSS signal, and a nadir-looking dual-band (1400–1427 MHz for the radiometer, and $L1$ for GNSS-R) left-hand circular polarization six-element patch antenna for the reflected GNSS signal and for the L-band microwave radiometer.

2) The radio frequency—front-end board (RF–FE) (#2 in Fig. 3) amplifies and conditions the signals. It is composed by different low noise amplifiers (LNA), filters, and a set of power splitters/switches to perform signal amplification and selection to the different SDR input channels.
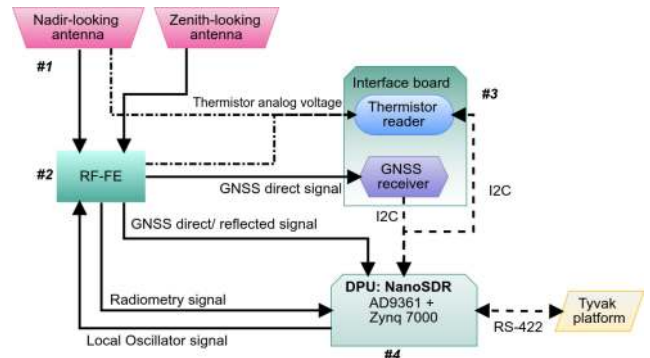
3) The interface board (IB) (#3 in Fig. 3) is a simple board used to interconnect the DPU, the RF–FE board, and the Novatel OEM719B GNSS receiver, used to geo-reference and time-tag the observables. This board also includes a circuit that acquires the temperature readings from the other payload modules and serves as a mechanical interface for the GPS receiver.

4) The data processing unit (DPU) (#4 in Fig. 3) is implemented through the NanoSDR module from GomSpace [30]; hence, it is both the SDR front end and the microprocessor unit. This unit is in charge of the data collection (analog-to-digital conversion), the execution of the FMPL-2 control software, and the execution of the processing software for both GNSS-R and L-band radiometry. The DPU is in charge of the communication with the platform on board computer (OBC) through a RS-422 link. This module is a mixture of an SDR, based on the AD9361 chip from analog devices, which is a RF front end broadly used for SDR, and it has two RX channels, sharing the local oscillator (LO), and two TX channels, also sharing the LO. The microprocessor unit of the DPU is based on a dual core ARM microprocessor, which is part of the Zynq7045 FPGA from Xilinx [31].

A. Antenna

The FMPL-2 payload is designed to work with two antennas: a nadir-looking dual-band passive antenna for both GNSS-R and L-band radiometry measurements, and a zenith-looking antenna for the GNSS direct signal acquisition.

On one hand, the zenith-looking antenna is based on a passive right-hand circularly polarized (RHCP) microstrip patch antenna centered at GPS $L1$ band, 1575.42 MHz. The zenith-looking antennas has a 3 dB beamwidth of $86.8°$ and a main lobe directivity of 6.85 dBi.

On the other hand, the nadir-looking antenna design is based on a six-element passive patch array (see Fig. 4), which resonates at two different bands: 1413 and 1575.42 MHz. Furthermore, the antenna does not contain any resistor that may generate additional thermal noise. Hence, the combiner used to merge the signals coming from the six elements is made of transmission lines only.
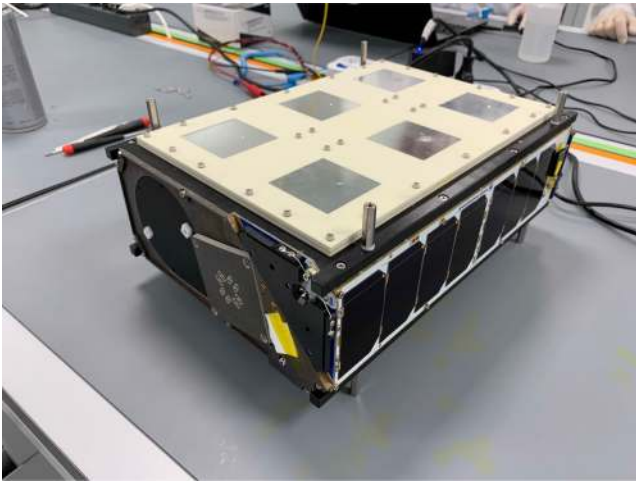
Fig. 4. UPC FMPL-2 six-element patch antenna array integrated into Tyvak's 6 U CubeSat platform (credit: Tyvak International [32]).
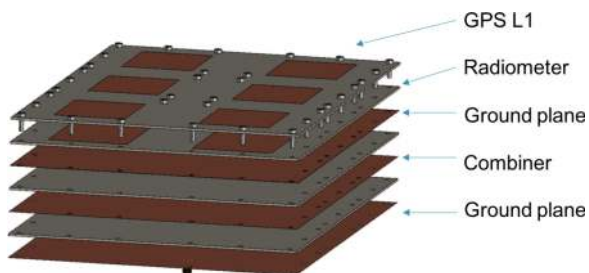

Fig. 5. FMPL-2 Nadir antenna design including its patches and combiner in the internal layers.

As detailed in Fig. 5, the antenna is designed in different layers. The first two layers contain the resonator patches, which have been designed to resonate at both 1413 and 1575.42 MHz. Those layers are then followed by a ground plane, and finally by the combiner layer, which takes the signal coming from the six patches, and combines them by means of a stripline-based combiner, which is afterwards routed to a single SMA connector.

B. Radio-Frequency Front End

Fig. 6 shows the signal routing from the nadir-looking antenna to a three-channel switch, which selects between the antenna input or any of the calibration loads (either the ACL or the matched load).

This input signal passes through a 20 dB isolator to improve the antenna return loss, and a high-IP3 LNA (19 dB of gain, 36 dBm of OIP3, and 0.37 dB of noise figure) that amplifies the signal before it is split in two channels: one for the Radiometer and the other one for the GNSS-R. Each of the channels is filtered using a surface acoustic wave (SAW) filter (60 MHz bandwidth for the radiometry channel and 2.4 MHz bandwidth for the GNSS channel), and then amplified using the same LNA model so as to have the gain matched. After all, the radiometric signal is routed to its output connector, while the GNSS signal passes through a two-channel switch, which can select between the nadir-looking path or the zenith-looking path.
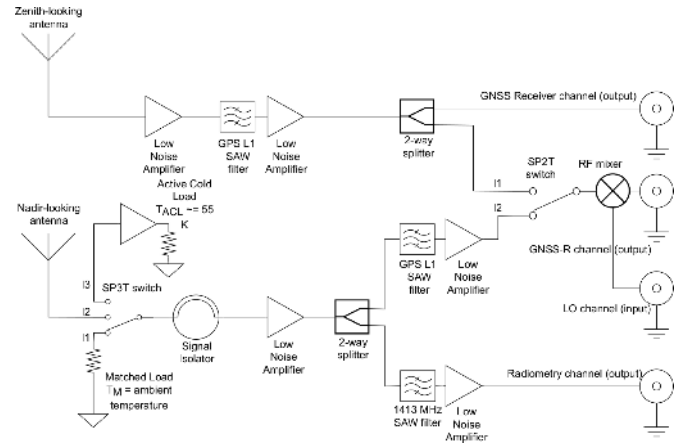

Fig. 6. RF–FE receiving chain.

TABLE I
RF–FE GAIN AND NOISE FIGURE (NF) REFERENCE

RF path	Gain [dB]	NF [dB]
Radiometry channel	56.2	0.96
Nadir-looking antenna to GNSS-R channel	52.9	1.14
Zenith-looking antenna to GNSS-R channel	53.3	0.60
Zenith-looking antenna to GNSS receiver channel	31.7	0.60

After the signal conditioning, the signal is routed to the DPU board, where the AD9361, the SDR chip (explained in detail in Section II-D), performs the analog-to-digital conversion. The AD9361 has two receiver inputs but with the same LO. Thus, in order to sample both GNSS *L1* and *L*-band radiometry signals at the same time and using the same AD9361 receiver, one of the two signals is down-converted to have the same central frequency. In this case, the GNSS signal is down-converted using an active mixer to the same frequency of the radiometer channel. To perform the down-conversion, one of the transmission channels of the AD9361 is used as LO of the external mixer (see Fig. 6).

The signal coming from the zenith-looking antenna undergoes also a two-stage amplification with a SAW filter in between, before it is connected to the GPS receiver, and to the switch of the GNSS channel from the AD9361 [33] receiver. Table I summarizes the different RF paths with their measured gains and noise figures.

C. Interface Board

The interface board is a simple two-layer board, the main purpose of which is to provide a mechanical and data interface for the GNSS receiver, the Novatel OEM719. The NanoSDR has a single I2C interface to connect any other peripheral; therefore, this interface is used to interface an I2C to the universal asynchronous receiver transmitter (UART) device, which is connected to the GNSS receiver COM interface.

In addition, this board contains a six-channel 14-bit analog-to-digital converter (ADC), which is controlled also by I2C interface, that is connected to different thermistors distributed in the nadir-looking antenna and the RF–FE board. The thermistors
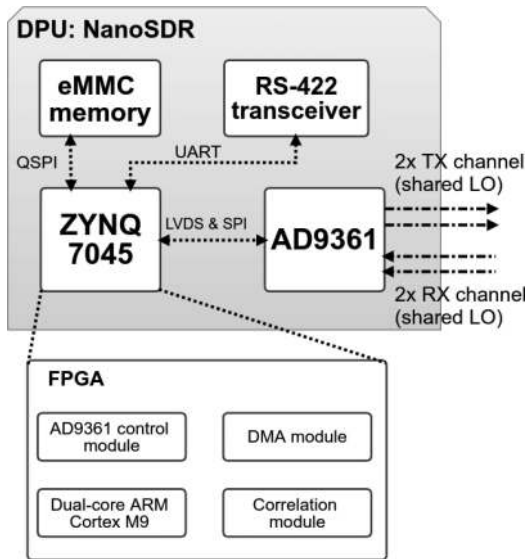
Fig. 7.   DPU detailed block diagram.

Fig. 8.   FMPL-2 software architecture is divided in two sections: User space (top part of the image) and Linux Kernel space (bottom of the image).

are distributed in the RF–FE board critical components, as the isolator, the SP3T switch, and the main LNA. Finally, two thermistors are placed in the inner face of the nadir-looking antenna, which is then used for calibration (see Section IV-B).

D. Data Processing Unit (DPU)

The DPU is the payload processing unit, and it is in charge of sampling the RF signal (i.e., RF down-conversion and IQ sampling), sending the IQ data to the ARM processor, applying the different processing algorithms (radiometry, GNSS-R), as well as the storage of the processor results. Moreover, this unit is in charge of retrieve, storage, and forward the payload housekeeping data (i.e., temperature measurements for both the signal conditioning board and the antennas), and to establish the communication with the platform OBC.

This board is based on the Nano-SDR from GomSpace, with flight heritage from the GOM-X4 mission. This module is composed by the TR-600 module [34], a two-channel 12-bit ADC, and two-channel digital-to-analog converter (DAC) based on the AD9361 chip. The TR-600 is controlled by the Nanomind Z7000 from GomSpace [30].

As detailed in Fig. 7, the DPU with its two main components: the Zynq7045 FPGA and the AD9361 chip. The FPGA implements a dual-core ARM, where all the code is implemented and executed. This module is interfaced to a eMMC memory, where the main code is stored, as well as the results of the FMPL-2 execution. In addition, the Zynq is connected to a RS-422 transceiver through UART, which is used to interface with the platform OBC. Moreover, the FPGA also implements a control module to acquire IQ samples and tune the AD9361. Finally, the FPGA implements the correlation module used by the cGNSS-R processor, which is connected to a DMA module to transfer the data from the ARM processor to the FPGA and viceversa.

The microcontroller unit of the DPU is a system on chip (SoC) based on an FPGA running a 667 MHz dual-core ARM
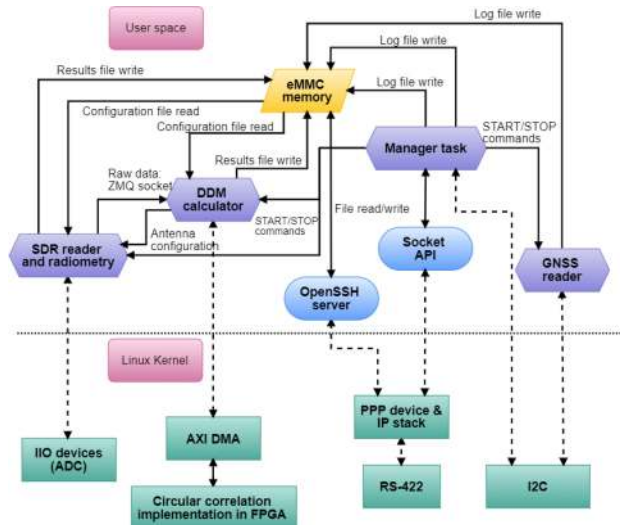
Cortex-A9 processor. The SoC runs a custom Linux Kernel from analog devices, which enables the DPU to easily configure, communicate, and stream I/Q data from the AD9361 chip to the user space, as the data interface between both modules is performed through a Linux standard library (LibIIO [35]), which is used to control industrial input/output peripherals, as the TR-600. The library uses a direct memory access (DMA) peripheral installed in the FPGA to transfer directly from the ADC/DAC to the ARM processor RAM memory.

E. Software Architecture

Moreover, the use of a Linux-based OS eases the communication between the platform computer, which is also running Linux, and the instrument computer. For the FSSCat mission, both computers are running a point-to-point protocol over RS-422, which at the end gives an IP address to the payload computer. Hence, the use of IP protocol gives the possibility to use a variety of already implemented network tools for communication such as: Secure Shell, File Transfer Protocol, TCP/IP stack, and the Linux socket API. The use of these validated tools reduces the overall mission risk and speeds up the development time.

The DPU runs several Linux user-applications split in different processes and also FPGA devices accessed through the Linux Kernel space in order to satisfy the payload requirements. As detailed in Fig. 8, the software developed is mostly running on top of the Linux user-space (rectangular diamond, in purple), which can be easily monitored and debugged. Other open-source tools (circular shape, in blue) are used to communicate internally between the different process and toward the platform, and finally some kernel modules (rectangular, in green) are used to perform all the functions.

To speed up the computation of the DDM, the DDM calculator uses some modules of the FPGA to perform the cross correlation of the GNSS. In order to transfer the data between the FPGA
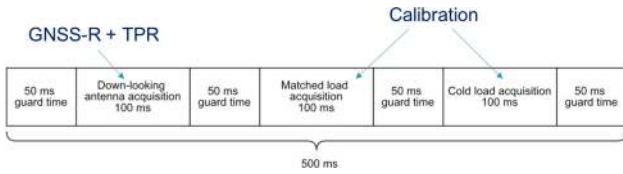
Fig. 9. Signal acquisition and processing steps to provide cGNSS-R and *L*-band radiometry at the same time.

TABLE II
STATE OF THE RF–FE SWITCHES (SEE FIG. 6) DURING THE
DIFFERENT ACQUISITIONS

Switch state during acquisition	SP3T position	SP2T position
Antenna acquisition	I2	I1: zenith-antenna path
		I2: nadir-antenna path
Matched load	I1	I2: nadir-antenna path
Active cold load	I3	I2: nadir-antenna path

fabric and the microcontroller memory, the software uses a kernel-space driver to interface with the DMA peripheral.

1) The SDR reader and the radiometry processor are merged into a single process. On one hand, the process is in charge of the communications through LibIIO with the SDR ADC. In addition, this process controls the switching through the different calibration loads. On the other hand, it also performs the radiometric observables calculation by integrating the square of the I/Q samples acquired for both GNSS and *L*-band radiometry channels. LibIIO is configured with two buffers: when one is full, it swaps to the next buffer, so as the user space can retrieve the first buffer contents. For this instrument configuration, each buffer can keep up to 50 ms of raw data.

2) The DDM calculator (or cGNSS-R processor) is in charge of performing the correlation of the GNSS (GPS and Galileo) signals. It is detailed in the following section.

3) The GNSS reader process is in charge of the configuration and communication with the Novatel OEM719B [36], the payload on-board GNSS receiver. The receiver streams *NMEA* messages as: *RANGE, BESTPOS, and SATVIS2*, which are including position, velocity, time, and pseudo-range measurements, which are then used to time-tag and geo-locate the GNSS-R and Radiometry data.

4) The manager task is the single point of communication with the platform computer and also process the platform commands or messages.

1) Signal Acquisition and Software Processing Steps: Both NanoSDR channels are sampled at the same time; hence, the cGNSS-R data and *L*-band radiometry data are exactly synchronized. Both channels need to be configured with the same parameters, which for the FMPL-2 case are set to 4.096 MSps and per channel.

The processing flowgraph is divided in blocks (see Fig. 9), with a repetition period of 500 ms, splitting the measurements in three steps, as listed in Table II.

In addition, each acquisition step has a guard period of the size of the acquisition buffer. Once a switch position is toggled,

some samples of the current buffer being streamed may contain data from both switch positions, for that reason the system waits for a buffer duration.

a) *Antenna measurement (100 ms):* For the radiometer, 100 ms of raw data are copied to user-space floating point complex buffer using the DMA peripheral. For the cGNSS-R, 40 ms of raw data are copied to the user-space 16-bit complex buffer, which is passed to the cGNSS-R processor through a ZMQ socket [37]. In addition, the power of the 40 ms of cGNSS-R signal is computed for calibration purposes.

b) *Matched load measurement (100 ms):* As in the antenna measurement case, the power is retrieved for both cGNSS-R and radiometry signal when the nadir-antenna is short circuited to the matched load.

c) *ACL measurement (100 ms):* As in the antenna measurement case, the power is retrieved for both cGNSS-R and radiometry signal when the nadir-antenna is connected to the ACL.

In order to implement the 50 ms guard times, the LibIIO is configured to continuously stream the ADC IQ data to a 50 ms buffer, which is read by the SDR process (see Section II-E2). The LibIIO uses up to four 50 ms buffers; thus, the SDR process has enough margin to make the radiometric processing during the guard times. In addition, the remaining 200 ms are used as guard time between each acquisition block, with another 50 ms at the end of all the acquisitions to retrieve and store to the eMMC memory all the results generated by the radiometer.

The purpose of retrieving a pair of calibration measurements for each antenna measurement is fundamental for these small spacecrafts, as temperature stability is not as good as in larger spacecrafts. For that reason, it is highly recommended [38] to increase the number of calibration points so as to compensate for any gain drift due to a temperature variation on the amplification chain.

2) SDR Reader and Radiometer Processor: This process is in charge of both controlling the SDR through LibIIO and to compute the power averaging of the I/Q samples for the radiometer. As shown in Fig. 10, this process is connected to the cGNSS-R processor through an interprocess communication pipe, from which the cGNSS-R processor can request data from either zenith antenna (for the direct signal path) or nadir antenna (for the reflected signal path).

The FMPL-2 radiometer covers the *L*-band radiometry (1400–1427 MHz) in 4 MHz wide sub-bands. The system is able to provide radiometric measurements at a rate of 2 Hz for its three sources: the nadir antenna, the ACL ($T_{cold} = 55$ K), and the matched load (T_{hot} = ambient temperature). Neglecting gain fluctuations, the theoretical radiometric sensitivity for this TPR is given in the following:

$$\Delta T = \frac{T_{sys}}{\sqrt{B \cdot \tau}} \qquad (2)$$

where $T_{sys} = T_A + T_R = 322$, with $T_R = 72$ K, and $T_A^{max} = 250$ K (pointing to thick ice), $B = 4$ MHz and $\tau = 0.1$ s, $\Delta T = 0.5$ K.
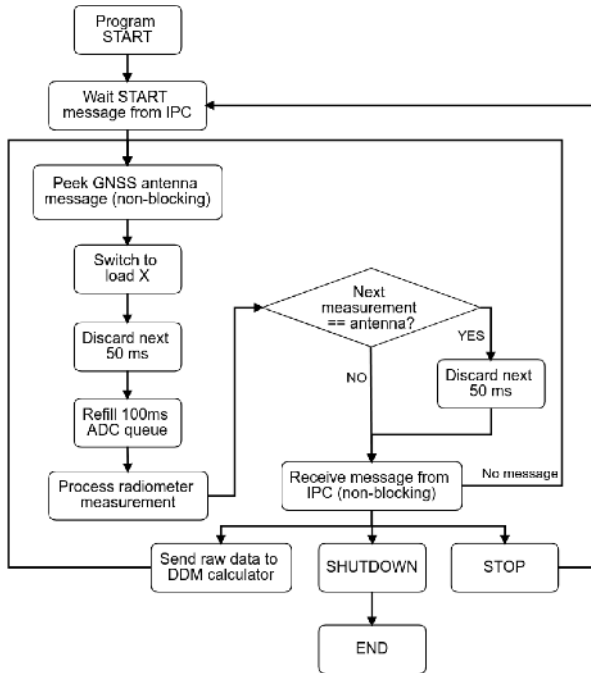
Fig. 10.　SDR reader and radiometer processor block diagram.

Fig. 11.　GNSS-R processor steps and flowgraph.

TABLE III
cGNSS-R INDIVIDUAL PROCESSING STEPS PARAMETERS

Step	Incoherent averaging	Doppler bin amount
Process Direct signal	10 ms	160 bins
Process Reflected signal	40 ms	20 bins
Track Reflected signal	40 ms	5 bins

Besides the radiometric measurement of each source, all the antenna measurements are evaluated with a statistical complex Kurtosis test [29], which performs a normality test to decide if the measurements contain any potential RFI. In case an interference is detected, the block with RFI is flagged for postprocessing on ground.

The Kurtosis values computed for each block are also downloaded as part of the instrument results data.

The complex signal kurtosis (CSK) is computed as in the following:

$$\text{CSK} = \frac{E[X-\mu]^4}{(E[X-\mu]^2)^2}. \tag{3}$$

A CSK equal to two means the I/Q samples received are Gaussian (i.e., thermal noise); therefore, the received samples do not contain any interference.

For the FMPL-2 case, the CSK is computed in block of 1 ms, which means that each 100 ms of I/Q data is split in 100 blocks and the CSK calculus is repeated for each of the 1 ms blocks. A CSK value is retrieved for each block and then averaged within all the blocks. The resulting CSK and the amount of blocks that contain a Kurtosis value out of 2 (± 0.2, which corresponds to a probability of false alarm of $6 \cdot 10^{-6}$ [39]) are tagged and downloaded for postprocessing.

3) cGNSS-R Processor: The cGNSS-R processor is divided in three different steps (see Fig. 11), the first step is a direct signal acquisition of all the visible PRNs corresponding to the GPS/Galileo satellites in view. The cGNSS-R processor requests the SDR reader process to switch feed into the GNSS ADC the zenith-looking signal.

The received signal is correlated against all visible PRNs using the parallel code phase search (PCPS) [40] algorithm,
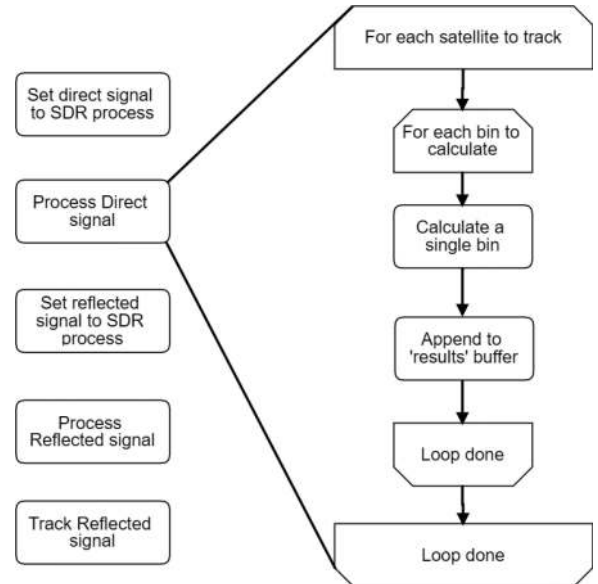
with and all possible Doppler shifts for the direct signal one. After the correlation, the instrument selects the PRN signals with the highest SNR, and it passes them to the next processing block, including the absolute Doppler shift of the signal. The *reflected signal acquisition* block repeats the process with a longer incoherent integration time, but with a narrower Doppler span, as the direct and reflected signals have a similar Doppler shift. Finally, this last block is repeated, but now with an even shorter Doppler span, in that way the processor is able to generate a DDM for the selected satellites before a new segment of I/Q data is received by the SDR process.

Table III summarizes the different parameters chosen by default in the different steps for both GPS *L1* C/A and Galileo E1 signals.

Each processing step of the cGNSS-R processor performs the GNSS signal acquisition by means of averaging incoherently the DDMs generated from a PCPS scheme [40].

In order to accelerate the GNSS signal acquisition, the PCPS implemented has been slightly modified from the original one [40]. Instead of performing the frequency shift of the acquired signal to perform the circular correlation, all code replicas are shifted. A total of 161 shifts per code is performed for all the available GPS and Galileo codes, which correspond to a total of ± 40 kHz Doppler span.

Furthermore, an FFT is performed to each frequency-shifted PRN and saved in the processor memory. Therefore, all
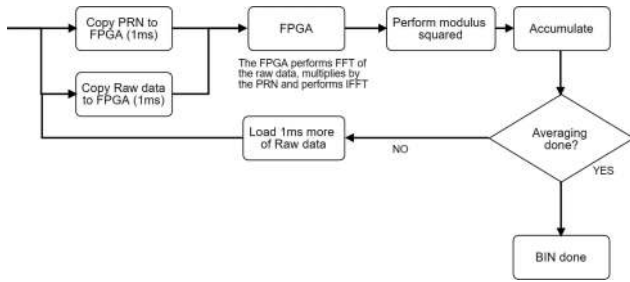
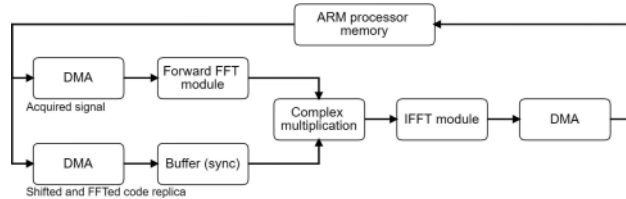Fig. 12. DDM process design inside the ARM processor.

Fig. 13. Circular correlation implemented in FPGA.

Fig. 14. FMPL-2 boards. (a) From left to right: 1) RF–FE board, 2) interface board (including Novatel OEM719B), and 3) GomSpace NanoSDR. (b) Boards already stacked in its final configuration during dry build fit-check. (c) FMPL-2 already integrated in its aluminum box during the ambient test campaign.

possible replicas are saved into the processor RAM memory as a 2-D matrix, ready to be cross-correlated with the incoming signal.

Part of the PCPS algorithm is executed in the FPGA fabric and other part of the algorithm is performed by the ARM processor. Fig. 12 details the implementation of the modified PCPS for FMPL-2. As seen, both the precomputed PRN and the incoming signal are copied into the FPGA fabric and then the FPGA performs the circular cross correlation. The data are then pulled out from the FPGA memory back to the ARM processor memory, the samples are modulus squared, and the ARM processor accumulates the circular cross-correlation result in a separate buffer. This process is repeated for each Doppler bin and for each satellite to be processed.

The communication between the FPGA fabric and the processor memory are implemented through DMA devices, once the data are received by both DMA in the FPGA, the correlation process starts (as detailed in Fig. 13) by performing the FFT of the incoming I/Q data, performing the complex multiplication of both signals, and then calculating the inverse FFT. The data are transferred back to the ARM memory through another DMA device.

Both complex number multiplication and FFT algorithm are given by Xilinx as an IP Core Block [31]. A specific circular correlation module is used for each GPS *L1* and Galileo E1 signal, as the coherent integration time for GPS *L1* is 1 ms and Galileo E1 is 4 ms (i.e., preprogrammed FFTs with different lengths for GPS *L1*, and Galileo E1).

The cGNSS-R processor takes packets of data from the SDR process once every 500 ms. From each packet, the processor is able to provide either 8 GPS-*L1* DDM/second or 2 Galileo-E1 DDM/s with up to 40 ms incoherent integration time with a default resolution of 100 delay bins, and 5 Doppler bins (user selectable, 500 Hz Doppler spacing and 0.25 C/A chips for GPS-*L1*). Note that, changing those parameters (i.e., increase
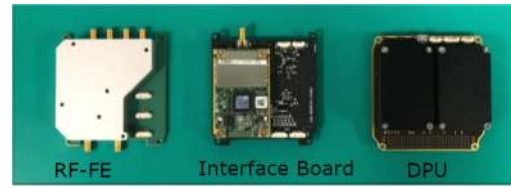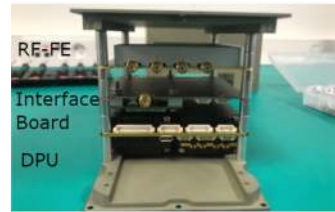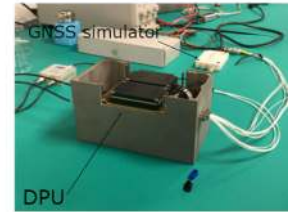
the Doppler bin resolution) impacts on the performance of the receiver. In addition, the chip resolution may be improved on ground by means of Fourier interpolation, as the signal is sampled satisfying the Nyquist criterion.

The incoherent integration time has been bounded to 40 ms so that the reflection does not get blurred [41] in the delay axis, and also several DDMs can be then stacked and accumulated after retracking the specular point on ground.

III. FMPL-2 IMPLEMENTATION AND TESTING PHASE

A. Implementation Overview

The FMPL-2 was implemented with mechanical compatibility with the PC104 CubeSat standard following the Proto-Flight Model (PFM) philosophy. The instrument fits inside a single CubeSat unit ($90 \times 90 \times 90$ mm^3), with a total weight of 1.4 kg (800 g from the aluminum box and 600 g from the electronics), with a peak power consumption of 8.5 W (5 V at 1.7 A). Fig. 14 shows the three main boards of the instrument during the dry build a fit-check test.

Even though the instrument fits inside a single CubeSat unit, it has been enclosed inside a ($175 \times 90 \times 90$ mm^3) anodized aluminum box to ease its integration and interfacing to the platform, perform the cable harnessing, etc.

B. Ambient Test Campaign

FMPL-2 ambient test campaign was split in two different sets, a preintegration test campaign and a postintegration test campaign. As the FMPL-2 implementation approach is a single PFM development, both the hardware and the software used need to be tested before and after the integration inside its aluminum case. In this case, the preintegration test campaign, even being part of the ambient test campaign, it was conducted during the implementation phase of the instrument development.

The anticipation of those tests before the final integration of the instrument was considered as a risk mitigation action, as in the case of any failure (i.e., protocol mismatch, wrong voltage level on the power lines, etc.) a corrective action can be taken without a major impact on the overall system schedule.

The preintegration campaign consisted of the validation of both the hardware and the software of the instrument with the following.

1) A platform interface emulator test: The communication channel was simulated using an RS-422 to USB adapter, which turns a regular laptop into a simulator of the platform OBC.

2) Platform interface test using an engineering model of the OBC: This test allows to validate the platform interface emulator. The purpose of this test is to check that the payload implementation that works with the platform interface emulator is valid also for the real platform. Note that, this test is not easily repeatable, as the platform OBC was at the platform integrator premises, in Torino, Italy, meanwhile the FMPL-2 was located at the UPC NanoSat Lab in Barcelona, Spain. The validation of the instrument performance relies on the platform emulator validation during the rest of the test campaign.

3) High-dynamics GNSS reception test: The entire instrument and both GNSS receiver and GNSS-R chain were tested with a high-dynamics direct signal for both direct and reflected channel. In addition, the high-dynamics direct signal was obtained from a SPIRENT simulator at the GNSS laboratory in ESA/ESTEC. The high-dynamics signal used during the test was recorded using a SDR for later play back in order to reproduce the test outputs in house.

Right after the finalization of the preintegration campaign, the payload enclosed in its aluminum box, glued, and tested again following the postintegration or ambient test campaign. In this case, the instrument went over the following tests again.

1) A platform interface emulator test: Same as during preintegration test campaign.

2) High-dynamics GNSS reception test: Using the recorded signal from the SPIRENT simulator at ESA/ESTEC Navigation Lab premises using a SDR.

3) RFI detection test: By adding a spurious signal right on top the *L*-band radiometry band and checking that the CSK algorithm is able to detect and report the interference.

4) Radiometer calibration load measurement: A set of measurements of both the matched load and the ACL to check the correct operation of the amplification and sampling chain.

Fig. 15 shows a snap-shot of two waveforms from the injected PRN 16 and PRN 23 of the GPS constellation.

The RFI detection test (see Fig. 16) was based on the injection of a CW tone centered at 1413 MHz with a power of -100 dBm, which produces an increase on the received power and also the Kurtosis indicator passes from 2, indicating the absence of interference, to almost zero, where the signal is totally contaminated by an interference.
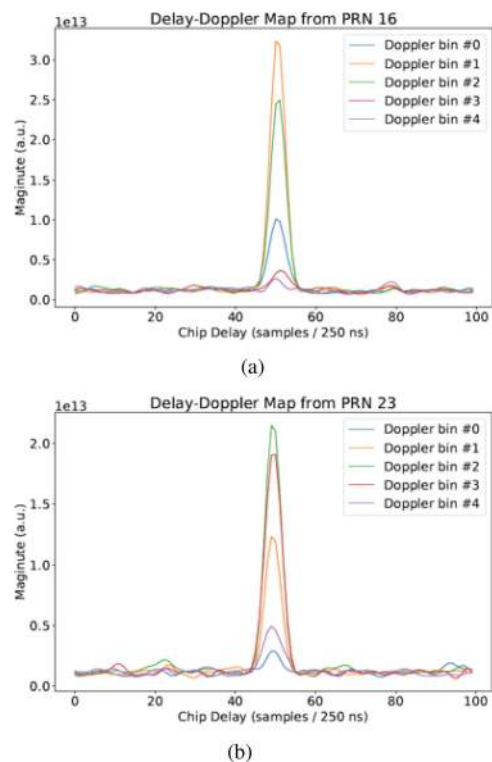

Fig. 15.   cGNSS-R processor output waveforms including five Doppler bins (frequency resolution = 500 Hz) of two of the in-view satellites during the ambient test campaign. (a) PRN 16 waveform with different Doppler cuts. (b) PRN 23 waveform with different Doppler cuts.
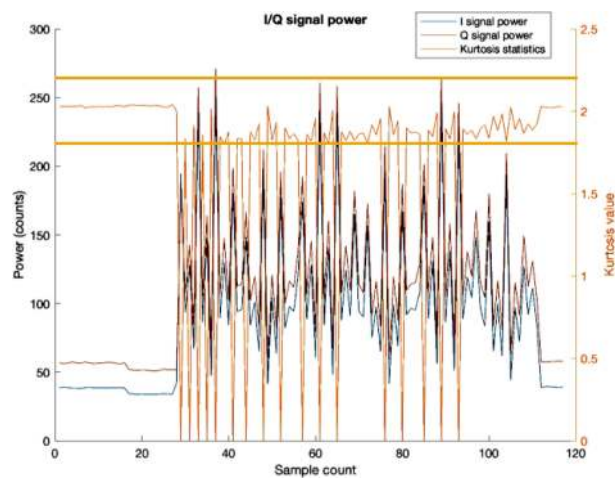

Fig. 16.   CW RFI detection test performed during the ambient test campaign, with the two horizontal lines in orange indicating the CSK limits for RFI detection (1.8 and 2.2).

To conclude the functional tests during the ambient test campaign, Fig. 17 shows the result of the radiometry calibration loads measurements over time and with respect to temperature variations, in both matched and ACL cases with a $R^2 = 0.95$ and a slope of -288 counts/$^\circ$C for the matched load and -136 counts/$^\circ$C for the ACL.

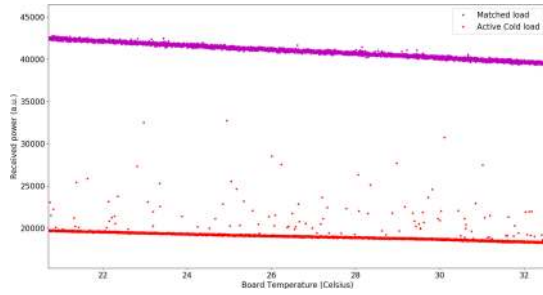Fig. 17. Radiometer calibration performed during the ambient test campaign.

Fig. 18. FMPL-2 Nadir antenna mounted in a 6-unit CubeSat model for radiation pattern measurement in UPC Antenna Lab anechoic chamber [42].

Fig. 19. Nadir antenna measured radiation pattern at 1413 MHz measurement in UPC Antenna Lab anechoic chamber [42]. (a) ZX cut ($E_\phi = 0°$). (b) ZY cut ($E_\phi = 90°$).

Aside from the electronics functional tests, the FMPL-2 nadir antenna module has been measured for both S_{11} parameter (see Fig. 18) and radiation pattern (see Figs. 19 and 20) at the UPC Antenna Lab anechoic chamber.

The nadir-looking antenna at the 1413 MHz has a directivity of 12.25 dB with a cross-track beamwidth of 36° and an along-track beamwidth of 58°.

The nadir-looking antenna at the 1575.42 MHz has a directivity of 12.22 dB with a cross-track 3 dB beamwidth of 35° and an along-track 3 dB beamwidth of 54°.
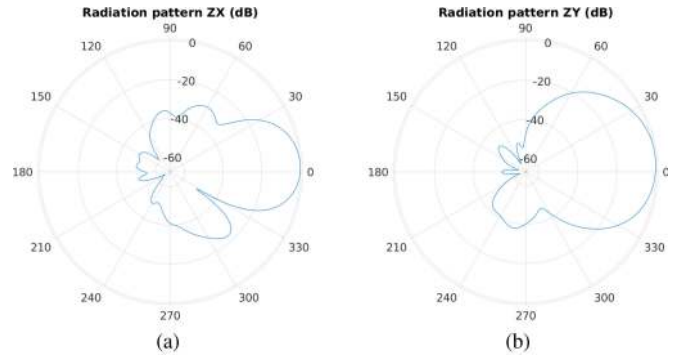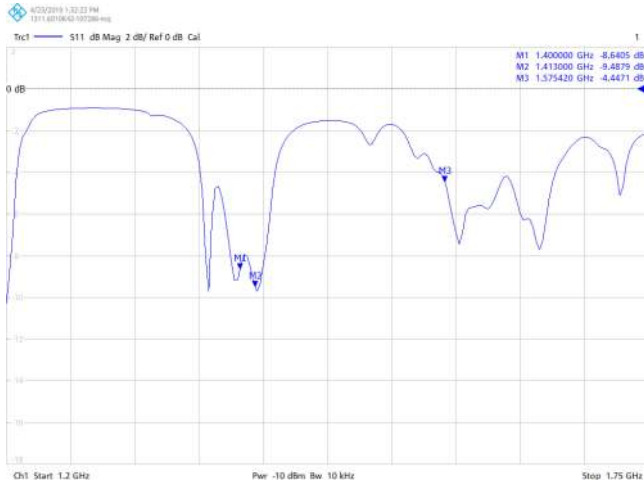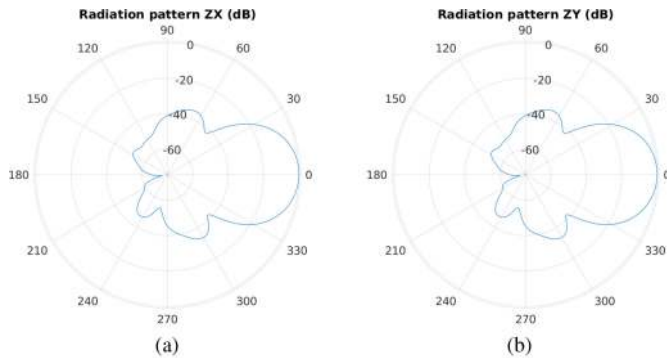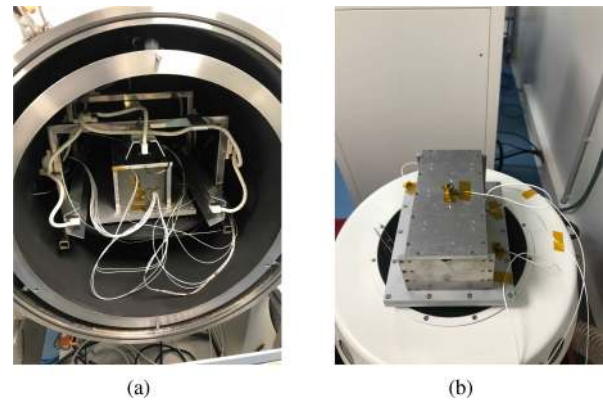

Fig. 20. Nadir antenna measured radiation pattern at 1575 MHz measurement in UPC Antenna Lab anechoic chamber [42]. (a) ZX cut ($E_\phi = 0°$). (b) ZX cut ($E_\phi = 90°$).

Fig. 21. Environmental test at UPC NanoSat-Lab facilities [5]. (a) FMPL-2 preparation for TVAC. (b) FMPL-2 preparation for vibration test at *Z*-axis.

C. Environmental Test Campaign

Once the payload has been functionally validated in ambient conditions, it shall be validated for the space environment, which means the following.

1) Thermal-vacuum cycling (TVAC) test: A total of four thermal cycles [see Fig. 21(a)] are performed in vacuum in order to verify the payload is able to operate and to dissipate through conduction and radiation of the internally generated heat toward the platform. According to the platform simulations [43], the FMPL-2 will be from 0 °C to 30 °C; therefore, the FMPL-2 has been tested with 10 °C of margin on both sides −10 °C and +40 °C.

2) Extended thermal-vacuum cycle calibration test: A part from the regular TVAC test, the FMPL-2 required a full temperature sweep to have a measurement of the radiometer output linearity with the temperature variation. As seen in Fig. 22, the FMPL-2 shows a small nonlinearity ($R^2 = 0.75$) at the ACL at low temperatures at the begging of the execution (at −10 °C). However, a linearity better than 2% is preserved ($R^2 > 0.95$) in the operational temperature range (from 0 °C to 40 °C), with a slope of −364 counts/°C for the matched load. The nonlinearity needs to be taken into account and a linear closed formula cannot be

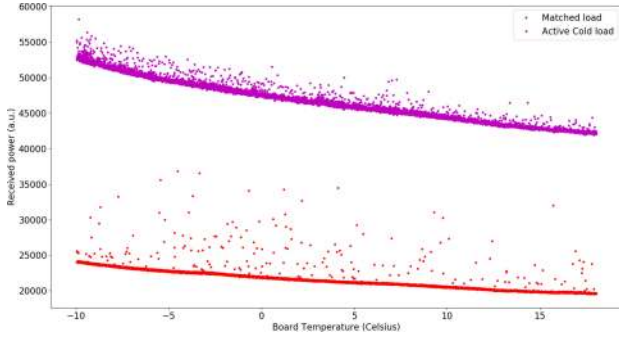Fig. 22.   *L*-band radiometry results of the extended TVAC calibration test. With a slope of -364 counts/°C and $R^2 = 0.95$ for the matched load and a slope of -154 counts/°C and $R^2 = 0.75$ for ACL measurement.
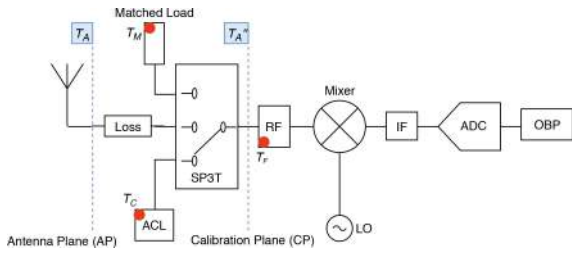

Fig. 23.   Simplified block diagram model of a single-channel microwave radiometer.

used to calibrate the radiometer; hence, a lookup table has to be used if the FMPL-2 is operated out of the operational temperature range. Note that, some outlier measurements are present in both matched load and ACL, which correspond to less than 1% of the measurements, and they can be filtered by means of a three- or five-element median filter.

3) *Vibration test:* During the launch, the spacecraft suffers from a hard random acceleration, which may cause the braking of a board, component, or a harnessing release. FMPL-2 has been tested [see Fig. 21(b)] with a shaking profile up to 12.4 g_{rms} in its three axis.

IV. FMPL-2 INSTRUMENT CALIBRATION

Calibration of the raw data is extremely important for both GNSS-R and *L*-band radiometer. Both systems require a perfect knowledge of the instrument gain and noise temperature to retrieve the absolute value of the observables (i.e., antenna temperature on the radiometer and power received on the GNSS-R).

A. Instrument Two-Point Calibration

As detailed in Section II-E1, the instrument performs the matched load and ACL measurements for calibration for both GNSS-R and *L*-band radiometer chains.

The simplified block diagram of a receiver for a single-channel radiometer is shown in Fig. 23. In our case, both instruments are calibrated independently; thus, the single-channel scheme is applied to both the GNSS-R and *L*-band chains, but with some of the components shared between them.

Both gain and noise temperature are retrieved for both chains using the two-point calibration method. This method consists of using the internal matched load and the ACL as standards in order to measure the receiver gain (4) and the receiver noise temperature (5) as follows:

$$G = \frac{v_{\text{hot}} - v_{\text{cold}}}{T_{\text{hot}} - T_{\text{cold}}} \tag{4}$$

$$T_R = \frac{T_{\text{hot}} v_{\text{cold}} - T_{\text{cold}} v_{\text{hot}}}{v_{\text{hot}} - v_{\text{cold}}} \tag{5}$$

where $T_{\text{hot}} = T_M$ is the physical temperature of the matched load, and T_{cold} is the noise temperature of the ACL at the calibration plane, which can be estimated from the following:

$$T_{\text{cold}} = T_{\text{ACL}} \frac{1}{L_s} + T_M \left(1 - \frac{1}{L_s}\right) \tag{6}$$

where T_{ACL} is the noise temperature of the ACL, measured on ground by the manufacturer at different ACL temperatures, as shown in the following equation:

$$T_{\text{ACL}} = 56\,\text{K} + 0.46\,\text{K/°C} \cdot (\text{T}_c - 25\,°\text{C}) \tag{7}$$

and $L_s = 0.24$ dB is the loss of the SP3T switch, measured on ground, and T_c is the physical temperature of the ACL.

B. Microwave Radiometer Calibration

The radiometer output power (8) is related to the antenna temperature at calibration plane T_A'' by

$$v = G(T_A'' + T_R) \tag{8}$$

where G is the transducer power gain (4), and T_R is the receiver noise temperature calculated in the previous section (5). The internal calibration estimates both parameters in order to solve this equation for T_A'' as

$$T_A'' = \frac{v}{G} - T_R. \tag{9}$$

Finally, the retrieved antenna temperature at the calibration plane shall be compensated for connector losses between the instrument and the antenna and for the ohmic losses of the antenna itself, as detailed in (10). Note that the physical temperatures is retrieved through thermal probes (PT-1000) installed in the nadir-looking antenna and in the RF–FE board near the SP3T switch. In addition, the estimates losses are given by design and also validated during the board implementation by the manufacturer as

$$T_A = \left(T_1 \cdot \left(1 - \frac{1}{L_{\text{Ant}}}\right) + T_2 \cdot (L_s - 1) - T_A'' \cdot L_s\right) \cdot L_{\text{Ant}} \tag{10}$$

where T_1 is the physical temperature of the antenna, T_2 is the temperature of the SP3T switch at the input of the calibration plane, L_s are the SP3T switch losses and L_{Ant} the antenna losses (taking into account the connection or cable losses).

C. GNSS-Reflectometer Calibration

Depending on the final application or data product, the GNSS-R instrument has to provide the delay between direct and reflected signals (delay altimetry), the reflectivity, which is proportional to the power ratio between the direct and the reflected signals (scatterometry), and those measurements retrieved from the shape of the DDM itself.

For example, the SIC products retrieved by FSSCat mission can be retrieved just by looking at the shape of uncalibrated DDMs. However, the reflectivity of the signal will be also retrieved to derive the SIT products from the *L*-band radiometry.

Each DDM cell output from the FMPL-2 is stored as normalized counts, which can be linked to the arriving signal power in Watts by using the following equation:

$$C = G \cdot (P_a + P_r + P_{\text{ref}}) \qquad (11)$$

where

1) C is the DDM value at a particular delay and Doppler frequency in counts output from the instrument at each delay/Doppler bin (for both nadir and zenith-looking antennas).
2) P_a is the thermal noise power generated by the antennas in Watts.
3) P_r is the thermal noise power generated by the instrument in Watts.
4) P_{ref} is the scattered signal power at the instrument in Watts at a particular delay and Doppler frequency.
5) G is the total instrument gain applied to the incoming signal in counts per Watts.

The terms C and P_{ref} are functions of delay (τ) and Doppler frequency (f_d), while P_a and P_r are assumed to be independent of the delay-Doppler bin the DDM. Every DDM includes 30 delay bins where signal power is not present, from which the noise floor level in counts can be estimated before the peak as

$$C_N = \frac{1}{N_{\text{dopplers}} \cdot 30} \sum_{d=1}^{N_{\text{dopplers}}} \sum_{i=1}^{30} C[d][i]. \qquad (12)$$

1) Calibration of the Signal Power: The DDM-received power can be calibrated by subtracting the noise power from the received signal, as in the following equations:

$$C_{\text{ref}} = C - C_N = G \cdot P_{\text{ref}} \qquad (13)$$

$$C_{\text{dir}} = C - C_N = G \cdot P_{\text{dir}} \qquad (14)$$

where C_{ref} and C_{dir} are the peak power of the DDM, and G can be calculated as for the microwave radiometer (4), as the matched and ACL measurements are also taken periodically for the GNSS receiving chain.

At the end, both powers are retrieved by isolating the power term as follows:

$$P_{\text{ref}} = \frac{C_{\text{ref}} - C_N}{G} \qquad (15)$$

$$P_{\text{dir}} = \frac{C_{\text{dir}} - C_N}{G}. \qquad (16)$$

2) Reflectivity Computation: FMPL-2 targets are ice and land, where the scattering has a coherent component larger than the incoherent (diffuse) one. Therefore, the DDM of the reflected signal looks like the direct one, with no tails (i.e., "boomerang" shape), but with a noisier background. In these conditions, a reflection coefficient can be computed for the coherent component at the specular reflection point. In addition, it is assumed that the transmitting antenna of the navigation satellite has a different directivity (G_T) for the transmitter–receiver path (θ_1, ϕ_1) and the transmitter-specular point path (θ_2, ϕ_2).

The next step is to compensate for the free-space propagation losses for both direct and reflected signals as follows:

$$P_{\text{dir}} = P_T \cdot G_T(\theta_1, \phi_1) \cdot \left(\frac{\lambda}{4\pi \cdot R_{T-R}}\right)^2 \cdot G_{\text{zenith}}(\theta_{\text{dir}}, \phi_{\text{dir}}) \qquad (17)$$

$$P_{\text{ref}} = P_T \cdot G_T(\theta_2, \phi_2) \cdot G_{\text{nadir}}(\theta_{\text{ref}}, \phi_{\text{ref}})$$
$$\cdot \left(\frac{\lambda}{4\pi \cdot (R_{T-\text{SP}} + R_{\text{SP}-R})}\right)^2. \qquad (18)$$

The reflection coefficient can now be estimated as follows:

$$\Gamma = \frac{P_{\text{ref}}}{P_{\text{dir}}} = \left(\frac{R_{T-\text{SP}} + R_{\text{SP}-R}}{R_{T-R}}\right)^2$$
$$\cdot \frac{G_{\text{zenith}}(\theta_{\text{dir}}, \phi_{\text{dir}})}{G_{\text{nadir}}(\theta_{\text{ref}}, \phi_{\text{ref}})} \cdot \frac{G_T(\theta_1, \phi_1)}{G_T(\theta_2, \phi_2)}. \qquad (19)$$

All the unknowns can be extracted from the satellite telemetry, as well as the radiation pattern from the antennas, which was measured in the UPC Antenna Lab anechoic chamber, as shown in Section III-B.

V. Conclusion

The FMPL-2 is a novel instrument that provides two passive microwave remote sensing techniques combined: *L*-band microwave radiometry and cGNSS-R. This article has presented the science case of the FSSCat mission and the design, implementation, and test of the FMPL-2, a miniature passive microwave remote sensor that may pave the path to large constellations of small passive microwave Earth Observation satellites.

Furthermore, the calibration methods for both microwave radiometry and GNSS-R instruments have been presented as well as the calibration parameters and temperature sensitivities derived during the environmental tests. This is needed to provide antenna temperatures and reflectivities.

At the time of writing this article, the FMPL-2 has been already integrated in Tyvak's platform and has undergone the environmental acceptance tests at the system level. The expected launch date of FSSCat is in Q2 2020 after a delay due to the failure of Vega VV15.

REFERENCES

[1] E. Kulu, World's largest database of nanosatellites, over 2500 NanoSats and CubeSats website. 2014. [Online]. Available: https://www.nanosats. eu/. Accessed on: Oct. 8, 2019.

[2] The CubeSat Program—California Polytechnic State University. Cubesat design specification rev. 13. 2015. [Online]. Available: http://www. cubesat.org/resources. Accessed: Oct. 7, 2019.

[3] A. Camps, "Nanosatellites and applications to commercial and scientific missions," in *Satellites and Innovative Technology [Working Title]*. London, U.K.: IntechOpen, Nov. 2019. [Online]. Available: https://doi.org/10. 5772/intechopen.90039

[4] A. Camps, "Nanosatellites and applications to commercial and scientific missions," in *Satellites and Innovative Technology*. London, U.K.: IntechOpen, 2019. [Online]. Available: https://www.intechopen.com/online-first/nanosatellites-and-applications-to-commercial-and-scientific-missions. Accessed: Dec. 12, 2019.

[5] UPC NanoSat-Lab website. 2018. [Online]. Available: https://nanosatlab. upc.edu. Accessed: Oct. 7, 2019.

[6] H. Carreno-Luengo *et al.*, "3Cat-2 An experimental nanosatellite for GNSS-R earth observation: Mission concept and analysis," *IEEE J. Sel. Topics Appl. Earth Observ. Remote Sens.*, vol. 9, no. 10, pp. 4540–4551, Oct. 2016.

[7] J. F. Munoz-Martin *et al.*, "3Cat-4: Combined GNSS-R, *L*-Band rtadiometer with RFI mitigation, and AIS receiver for a I-unit cubesat based on software defined radio," in *Proc. IEEE Int. Geosci. Remote Sens. Symp.*, Jul. 2018, pp. 1063–1066.

[8] "Cosine measurement systems," Hyperscout from Cosine website. 2016. [Online]. Available: https://hyperscout.nl/. Accessed: Dec. 2018.

[9] A. Alonso-Arroyo, V. U. Zavorotny, and A. Camps, "Sea ice detection using U.K. TDS-1 GNSS-R data," *IEEE Trans. Geosci. Remote Sens.*, vol. 55, no. 9, pp. 4989–5001, Sep. 2017.

[10] L. Kaleschke, X. Tian-Kunze, N. Maaß, M. Mäkynen, and M. Drusch, "Sea ice thickness retrieval from SMOS brightness temperatures during the Arctic freeze-up period," *Geophysical Res. Lett.*, vol. 39, no. 5. [Online]. Available: https://agupubs.onlinelibrary.wiley.com/doi/abs/10. 1029/2012GL050916

[11] V. U. Zavorotny, S. Gleason, E. Cardellach, and A. Camps, "Tutorial on remote sensing using GNSS bistatic radar of opportunity," *IEEE Geosci. Remote Sens. Mag.*, vol. 2, no. 4, pp. 8–45, Dec. 2014.

[12] R. Kwok, "Satellite remote sensing of sea-ice thickness and kinematics: A review," *J. Glaciol.*, vol. 56, no. 200, p. 1129–1140, 2010.

[13] M. Piles *et al.*, "Downscaling SMOS-derived soil moisture using MODIS visible/infrared data," *IEEE Trans. Geosci. Remote Sens.*, vol. 49, no. 9, pp. 3156–3166, Sep. 2011.

[14] G. Portal *et al.*, "A spatially consistent downscaling approach for SMOS using an adaptive moving window," *IEEE J. Sel. Topics Appl. Earth Observ. Remote Sens.*, vol. 11, no. 6, pp. 1883–1894, Jun. 2018.

[15] F. Martin *et al.*, "Mitigation of direct signal cross-talk and study of the coherent component in GNSS-R," *IEEE Geosci. Remote Sens. Lett.*, vol. 12, no. 2, pp. 279–283, Feb. 2015

[16] H. Carreno-Luengo, H. Park, A. Camps, F. Fabra, and A. Rius, "GNSS-R derived centimetric sea topography: An airborne experiment demonstration," *IEEE J. Sel. Topics Appl. Earth Observ. Remote Sens.*, vol. 6, no. 3, pp. 1468–1478, Jun. 2013.

[17] P. Jales, "Spaceborne receiver design for scatterometric GNSS reflectometry," Ph.D. thesis, Faculty Eng. Physical Sci., Univ. Surrey, Surrey, U.K., 2012.

[18] V. U. Zavorotny and A. G. Voronovich, "Scattering of GPS signals from the ocean with wind remote sensing application," *IEEE Trans. Geosci. Remote Sens.*, vol. 38, no. 2, pp. 951–964, Mar. 2000.

[19] S. Katzberg and J. Garrison, "Utilizing GPS To determine ionospheric delay over the ocean," NASA Tech. Memorandum 4750, NASA, Washington, DC, USA, 1996.

[20] A. Camps, "Spatial resolution in GNSS-R under coherent scattering," *IEEE Geosci. Remote Sens. Lett.*, vol. 17, no. 1, pp. 32–36, Jan. 2020.

[21] F. Martin *et al.*, "Mitigation of direct signal cross-talk and study of the coherent component in GNSS-R," *IEEE Geosci. Remote Sens. Lett.*, vol. 12, no. 2, pp. 279–283, Feb. 2015.

[22] Z. Yongchao, K. Yu, J. Zou, and J. Wickert, "Sea ice detection based on differential delay-Doppler maps from UK TechDemoSat-1," *Sensors*, vol. 17, 07 2017, Art. no. 1614.

[23] S. S. T. Limited, "MERRByS product manual v3," 2017. [Online]. Available: http://merrbys.co.uk/wp-content/uploads/2017/07/MERRByS-Product-Manual-V3.pdf. Accessed: Jan. 2019.

[24] N. Rodriguez-Alvarez, B. Holt, S. Jaruwatanadilok, E. Podest, and K. C. Cavanaugh, "An Arctic sea ice multi-step classification based on GNSS-R data from the TDS-1 mission," *Remote Sens. Environ.*, vol. 230, 2019, Art. no. 111202.

[25] A. Camps, M. Vallċllossera, H. Park, G. Portal, and L. Rossato, "Sensitivity of TDS-1 GNSS-R reflectivity to soil moisture: Global and regional differences and impact of different spatial scales," *Remote Sens.*, vol. 10, no. 11, 2018, Art. no. 1856. [Online]. Available: https://www.mdpi.com/2072-4292/10/11/1856

[26] eoPortal "Directory," Cyclone GNSS mission description website. [Online]. Available: https://directory.eoportal.org/web/eoportal/satellite-missions/c-missions/cygnss. Accessed: Jan. 2019.

[27] C. Gabarro, A. Turiel, P. Elosegui, J. A. Pla-Resina, and M. Portabella, "New methodology to estimate Arctic sea ice concentration from SMOS combining brightness temperature differences in a maximum-likelihood estimator," *The Cryosphere*, vol. 11, no. 4, pp. 1987–2002, 2017.

[28] European Space Agency. Eight years of SMOS Arctic sea ice thickness level now available from SMOS Data dissemination portal. 2018. [Online]. Available: https://earth.esa.int/web/guest/missions/esa-operational-eo-missions/smos/ne ws/-/article/eight-years-data-of-smos-arctic-sea-ice-thickness-level-now-avail able-from-smos-data-dissemination-portal. Accessed: Nov. 11, 2019.

[29] J. Querol, R. Onrubia, A. Alonso-Arroyo, D. Pascual, H. Park, and A. Camps, "Performance assessment of time-frequency RFI mitigation techniques in microwave radiometry," *IEEE J. Sel. Topics Appl. Earth Observ. Remote Sens.*, vol. 10, no. 7, pp. 3096–3106, Jul. 2017.

[30] GomSpace Group AB. GomSpace Software Defined Radio product description website. [Online]. Available: https://gomspace.com/shop/payloads/software-defined-radio.aspx. Accessed: Oct. 7, 2019.

[31] Xilinx. "Fast Fourier transform (FFT)," 2018. [Online]. Available: https://www.xilinx.com/products/intellectual-property/fft.html

[32] Tyvak International, "Tyvak Internal: A Terran Orbital Corporation official website," [Online]. Available: https://www.tyvak.eu. Accessed: Oct. 21, 2019.

[33] Analog Devices. "Analog Devices AD9361 datasheet," 2016. [Online]. Available: https://www.analog.com/media/en/technical-documentation/data-sheets/AD9361.pdf. Accessed: Oct. 7, 2019.

[34] GomSpace Group AB. "TR-600: Radio daughterboard for use in SDR platforms," [Online]. Available: https://gomspace.com/shop/subsystems/communication-systems/nanocom-tr-600.as px. Accessed: Oct. 7, 2019.

[35] Analog Devices. "Analog devices LibIIO reference," 2014. [Online]. Available: https://github.com/analogdevicesinc/libiio. Accessed: Dec. 2018.

[36] Novatel. "OEM719 Multi-Frequency GNSS Receiver," [Online]. Available: https://www.novatel.com/products/gnss-receivers/oem-receiver-boards/oem7-receivers/oem719/. Accessed: Oct. 7, 2019.

[37] S. McCoy and L. Naude, "ZMQ reference guide website," [Online]. Available: http://zeromq.org/. Accessed: Jun. 2019.

[38] M. A. Goodberlet and J. B. Mead, "Two-load radiometer precision and accuracy," *IEEE Trans. Geosci. Remote Sens.*, vol. 44, no. 1, pp. 58–67, Jan. 2006.

[39] J. Querol, "Radio frequency interference detection and mitigation techniques for navigation and Earth observation," Ph.D. thesis, Dept. de Teoria del Senyal i Comunicacions, Technical Univ. Catalonia, Barcelona, Spain. 2018. [Online]. Available: https://upcommons.upc.edu/handle/2117/125028. Accessed: Oct. 15, 2019.

[40] R. Khan, S. U. Khan, R. Zaheer, and S. Khan, "Acquisition strategies of GNSS receiver," in *Proc. Int. Conf. Comput. Netw. Inf. Technol.*, Jul. 2011, pp. 119–124.

[41] H. Park, D. Pascual, A. Camps, F. Martin, A. Alonso-Arroyo, and H. Carreno-Luengo, "Analysis of spaceborne GNSS-R delay-Doppler tracking," *IEEE J. Sel. Topics Appl. Earth Observ. Remote Sens.*, vol. 7, no. 5, pp. 1481–1492, May 2014.

[42] UPC AntennaLab anechoic chamber. [Online]. Available: https://www.tsc.upc.edu/en/facilities/anechoic-chamber. Accessed: Oct. 21, 2019.

[43] Tyvak International, Tyvak Internal Communication, 2018.

[44] A. Camps *et al.*, "Fsscat, the 2017 copernicus masters' "ESA sentinel small satellite challenge" winner: A federated polar and soil moisture tandem mission based on 6U cubesats," in *Proc. IEEE Int. Geosci. Remote Sens Symp.*, Jul. 2018, pp. 8285–8287.

Joan Francesc Munoz-Martin (Student Member, IEEE) was born in Mallorca in 1992. He received the M.Sc. degree in telecommunications engineering from the Universitat Politècnica de Catalunya – UPC BarcelonaTech, Barcelona, Spain. He is currently working toward the Ph.D degree for the Universitat Politècnica de Catalunya.

He joined the NanoSat Lab, Universitat Politècnica de Catalunya, in 2013 as a Communications System Engineer for the 3Cat-1 mission and has been involved in all its missions ever since. He participated in ESA's BEXUS 19 campaign, with a proof of concept of the GNSS-R spaceborne technology integrated in 3Cat-2. He also led the OBDH, TT&C, and Ground Operations for 3Cat-2 mission. He is currently the lead Software and Payload Engineer of 3Cat–4 mission, part of *Fly Your Satellite!* program from the ESA. Moreover, he is the Payload Manager of the GNSS-R and L-band radiometer microwave passive payload of the ESA S3 FSSCat mission. In addition, he is the payload responsible for the circular polarization GNSS-R experiment of the MOSAiC campaign in the arctic sea.

Joan Adrià Ruiz-de-Azúa Ortega (Student Member, IEEE) was born in Barcelona, Spain. He received the degrees in aerospace engineering from Supaero, Toulouse, France and in telecommunications engineering from Unversitat Politècnica de Catalunya, Barcelona, Spain, in 2015. He also received the M.S. degrees in network protocols from Supaero, in 2015. He was awarded with the Best M.S. Thesis on Critical Communications from the Official Spanish Telecommunications Chartered Institute in 2016. He is currently working toward the Ph.D. degree with the Universitat Politècnica de Catalunya.

He has participated in different projects of ground segment for Ariane 5 and Ariane 6 programs in GTD company, in collaboration with CNES and ESA. He is currently participating in the *Fly Your Satellite!* program from the ESA, and he is the member of the FSSCat project, which is the winner of the ESA Sentinel Small Sat (S^3) Challenge of the Copernicus Masters Competition. His research interests include satellite architectures, satellite networks, cognitive networks, Internet of Things, 5G networks, deep learning, and embedded software.

Lara Fernandez Capon (Student Member, IEEE) was born in Barcelona, Spain. She received the degree in telecommunications engineering from Universitat Politècnica de Catalunya, Barcelona, Spain, in 2017. She also received the M.Sc. degree in telecommunications engineering from Universitat Politècnica de Catalunya, in 2019. She is currently working toward the Ph.D. degree with the Universitat Politècnica de Catalunya.

She is currently participating in the *Fly Your Satellite* program from the ESA, and she is the member of the FSSCat project, which is the winner of the ESA Sentinel Small Sat (S^3) Challenge of the Copernicus Masters Competition. Her research interests include Internet of Things, 5 G networks, satellite networks, communication systems, and antenna design.

Adriano Camps (Fellow, IEEE) received the degree in telecommunications engineering and the Ph.D. degree in telecommunications engineering from the Universitat Politecnica de Catalunya (UPC), Barcelona, Spain, in 1992 and 1996, respectively.

He is currently a Full Professor with Telecom Barcelona, Universitat Politecnica de Catalunya, Barcelona, Spain. He is the Scientific Coordinator of the CommSensLab "Maria de Maeztu" Excellence Research Unit, Universitat Politecnica de Catalunya. He has authored and coauthored more than 180 journal papers in peer-reviewed journals, more than 350 international conference presentations, 7 book chapters, 1 book, and more than 397 international conference presentations, holds 10 patents, and has advised 23 Ph.D. students (more than 8 on-going), and more than 120 final project and M.Eng. theses. His research interests include synthetic aperture microwave radiometry (i.e., ESA SMOS Earth Explorer Mission), GNSS-reflectometry, nanosats as affordable platforms to test new remote sensors and communication systems, and radio-frequency interference detection and mitigation systems for microwave radiometers and GNSS receivers.

Prof. Camps was the President of the IEEE Geoscience and Remote Sensing Society in 2017 and 2018.